



One-step synthesis of nanostructured Pd-doped mixed oxides $\text{MO}_x\text{-CeO}_2$ ($\text{M} = \text{Mn, Fe, Co, Ni, Cu}$) for efficient CO and C_3H_8 total oxidation

Jin-Yong Luo, Ming Meng*, Jin-Song Yao, Xin-Gang Li, Yu-Qing Zha, Xitao Wang, Tian-Yong Zhang

Tianjin Key Laboratory of Applied Catalysis Science and Engineering, Department of Catalysis Science and Technology, School of Chemical Engineering and Technology, Tianjin University, Tianjin 300072, PR China

ARTICLE INFO

Article history:

Received 27 May 2008

Received in revised form 27 July 2008

Accepted 14 August 2008

Available online 26 August 2008

Keywords:

Palladium

Ceria

CO oxidation

Propane oxidation

Synergism

Mechanism

ABSTRACT

A series of nanostructured Pd-doped mixed oxides $\text{MO}_x\text{-CeO}_2$ ($\text{M} = \text{Mn, Fe, Co, Ni, Cu}$), with uniform mesoporous structure and large surface area exceeding $115 \text{ m}^2 \text{ g}^{-1}$, were synthesized in one step by a surfactant-assisted co-precipitation. Their catalytic performance was investigated using total oxidation of CO and C_3H_8 as the model reactions. The results show that, a synergism exists between even trace amounts of exposed Pd and 3d-transition metal oxides for CO oxidation, whereas such an effect is absent for C_3H_8 oxidation. In situ diffuse reflectance infrared spectroscopy (DRIFTS) study reveals that the synergistic essential for CO oxidation should be the interaction-assisted generation of active oxygen species between Pd and MO_x , which react readily with CO, forming bidentate carbonate (1587 and 1285 cm^{-1}) as intermediates. Moreover, structural characterization results indicate that a solid solution is formed between CeO_2 and Mn_2O_3 or Fe_2O_3 , resulting in the very strong interaction between Pd and MO_x , as well as the greatly improved CO oxidation. The light-off temperatures for Pd-doped Mn and Fe-containing catalysts, as compared with the Pd-free catalysts, are decreased by more than 70 and 100 °C, respectively. In particular, a CO conversion as high as 80% can be achieved even at room temperature on Pd-doped Mn-containing catalyst. While for C_3H_8 oxidation, the C–H bond activation, but not the oxygen activation, plays a crucial role. The C–H bond activation ability of the catalysts is largely determined by the d-electron configurations of the M cations. A 'double-peak' phenomenon can be derived with the increase of d-electron number.

© 2008 Elsevier B.V. All rights reserved.

1. Introduction

The control of noxious emissions from automobiles is one of the most urgent and compelling problems faced by nearly every country in the world. It has been reported that during the cold-start transients, a considerable amount (50–80%) of CO and hydrocarbons (HCs) is released into the air despite the application of the three-way catalysts (TWCS) [1]. It is therefore highly recommended to explore catalysts with excellent low-temperature oxidation activity for the removal of CO and HC.

Currently, noble metal catalysts, especially platinum group catalysts, represent the state-of-art in internal combustion engine emission technology, but the high price and low availability limit their application. In such situation, some base metal oxides attract much attention since they are very active as well. For example, it has been reported that Co_3O_4 catalysts can exhibit high activity for CO oxidation as low as –63 °C and for propane activation even

under ambient conditions [2,3]. However, the stability presents a challenge. Due to the depletion of the active oxygen species, these catalysts suffer from relatively quick deactivation. In order to lower the catalyst cost and maintain the sustainable high activity at the same time, some researchers found that, promotion of base metal oxides with even a small amount of noble metals can greatly improve their steady-state oxidation activities, such as in the supported Pd-(CrO_x , MnO_x , Fe_2O_3 , Co_3O_4 , LaCoO_3) [4–11], Pt(-Pd)- Co_3O_4 [12–14]. The support selection is another important aspect. For the most frequently used support-Al₂O₃ with high surface area, the strong metal oxide-support interaction, like the formation of the M–O–Al linkage, is detrimental to the propane oxidation [15]. As regarding CeO_2 , its strong interaction with metal oxides MO_x can weaken the M–O bond [16], which is favorable to the oxidation activity by contrast. On this basis, it is desirable to develop mixed oxides $\text{MO}_x\text{-CeO}_2$ promoted by a small amount of noble metals.

Recently, $\text{Co}_3\text{O}_4\text{-CeO}_2$ catalysts with high surface area and mesoporous structure were prepared, using a template method or co-precipitation in the presence of surfactant cetyltrimethyl ammonium bromide (CTAB) as described elsewhere [17]. After conventional impregnation with Pd, its surface area is remarkably

* Corresponding author. Tel.: +86 22 2789 2275; fax: +86 22 2789-2275.
E-mail address: mengm@tju.edu.cn (M. Meng).

decreased because of the partial pore blocking and the enhanced CeO₂ crystallization. So what about the synthesis of the Pd-containing mixed oxides by one-step co-precipitation? In this case, the preparation procedures can be reduced, and more importantly, the high surface area can be maintained. The main concern is probably the encapsulation of the precious metals in the volume, which may result in the inefficient utilization of these metals. But some new observations indicate that even the totally-encapsulated catalysts exhibit excellent catalytic activity, such as the Pt-in-CeO₂ [18,19] and Ir-in-CeO₂ catalysts [20]. In these catalysts, the encapsulation structure can generate very strong or even maximum metal–ceria interaction, weakening the surface Ce–O bond and forming more reactive oxygen species. On the basis of enhanced component interaction, it seems promising to prepare excellent low-temperature oxidation catalysts by one-step co-precipitation.

Consequently in this work, a series of Pd-promoted mixed oxide catalysts MO_x–CeO₂ (M = Mn, Fe, Co, Ni, Cu) were synthesized in the presence of CTAB by one-step co-precipitation. The structural properties, redox behaviors and catalytic performance of the catalysts for CO and C₃H₈ oxidation were carefully investigated and correlated. The goal of present study was to explore new preparation method and to gain some insights into the reaction mechanisms for CO and C₃H₈ oxidation, in order to design optimal oxidation catalysts used for the removal of cold-start emission.

2. Experimental

2.1. Catalyst preparation

The Pd-promoted MO_x–CeO₂ mixed oxides (atomic ratio: M/Ce = 3/7, M = Mn, Fe, Co, Ni or Cu) were prepared by the one-step co-precipitation in the presence of CTAB, as described elsewhere [17]. Appropriate amounts of PdCl₂, MCl_x·yH₂O (MnCl₂·4H₂O, FeCl₃·6H₂O, CoCl₂·6H₂O, NiCl₂·6H₂O, CuCl₂·2H₂O), CeCl₃·7H₂O (Shanghai Chemical Reagents), and CTAB (Fuchen Chemical Reagents Factory) were dissolved in distilled water (molar ratio: CTAB/(M + Ce) = 0.8), then aqueous solution of NaOH (2 M) was added dropwise until the pH arrived at ca. 11. After continuous stirring for 2 h, the obtained suspension was transferred to a Teflon-sealed autoclave and hydrothermally aged at 120 °C for 48 h. After filtration, washing and drying, the powder was calcined in air at 500 °C for 4 h. The catalysts were denoted as PdCeM. For comparison, the non-promoted mixed oxides, Pt or Au-promoted Co₃O₄–CeO₂ (precursor: H₂PtCl₆·6H₂O or HAuCl₄·3H₂O), and Pd–CeO₂ catalysts were prepared by the same method as well. All the precious metals have a 0.5% weight loading. The actual composition of the catalyst was analyzed by atomic absorption spectroscopy (AAS, Hitachi 180-80).

2.2. Catalyst characterization

Surface area, pore volume and pore size distribution were measured by nitrogen adsorption/desorption at 77 K using a Quantachrome QuadraSorb SI instrument. The samples were degassed at 300 °C for 8 h before experiments. The specific surface area (S_{BET}) was determined from the linear part of the adsorption curve. The pore diameter distribution was calculated from the desorption branch using the BJH formula.

X-ray diffraction (XRD) patterns were recorded on an X'pert Pro rotatory diffractometer (PANalytical Company) using Co K_α radiation ($\lambda = 0.1790 \text{ nm}$) at 40 kV and 40 mA. The average crystallite size of CeO₂ was calculated by using Scherrer equation from the line broadening corresponding to crystal plane (1 1 1) without incorporating microstrain effects.

X-ray photoelectron spectra (XPS) were recorded on a PHI-1600 ESCA spectrometer using Mg-K_α radiation (1653.6 eV). The binding energies were calibrated using C1s peak of contaminant carbon (B.E. = 284.6 eV) as standard.

TEM images were obtained by using a Philips Tecnai G²F20 system operating at 200 kV. The sample was ultrasonically suspended and deposited on a carbon film supported on a copper grid.

Temperature programmed reduction by H₂ (H₂-TPR) was performed on a Thermo-Finnigan TPDRO 1100 instrument with a thermal conductivity detector (TCD). Before detection, the gas was purified by a solid trap containing CaO + NaOH materials in order to remove the H₂O and CO₂. The quartz tube reactor was loaded with 50 mg sample in powder form and heated from room temperature to 900 °C in 5% H₂/N₂ mixture with a flow rate of 20 ml min⁻¹. By replacing the 5% H₂/N₂ with 5% CO/He, the CO-TPR tests were also carried out. After the sample was reduced by 5% H₂/N₂ from room temperature to 500 °C and held for 10 min, temperature programmed oxidation (TPO) tests were performed from room temperature to 900 °C in 6% O₂/He flow at a rate of 20 ml min⁻¹.

In situ diffuse reflectance infrared spectroscopy (DRIFTS) measurement was performed on a Nicolet Nexus spectrometer equipped with a MCT detector cooled by liquid nitrogen. First, the sample powder (30 mg) was treated in situ at 300 °C in 6% O₂/He with a flow rate of 50 ml min⁻¹. After cooling to room temperature in 6% O₂/He, a background spectrum was collected for spectra correction. Subsequently, pure CO was further introduced to the in situ chamber for 5 min adsorption, accounting for a concentration of 3% in the gas mixture. The spectra were collected accumulating 32 scans at a resolution of 2 cm⁻¹, and displayed in Kubelka–Munk unit.

2.3. Catalytic activity measurement

The catalytic activity measurement was carried out in a continuous fixed-bed quartz tubular reactor (i.d. 8 mm) mounted in a tube furnace. The temperatures of both the furnace and the catalyst bed were measured by thermocouples. The feed gas mixture, consisting of 1% CO and 5% O₂, or 0.5% C₃H₈ and 5% O₂, balanced by N₂, was fed to the catalyst bed (20–60 mesh, 600 mg) without diluent at a weight hourly space velocity (WHSV) of 15,000 ml g⁻¹ h⁻¹. The effluent gas from the reactor was analyzed by a gas chromatograph (BFS SP-3430) equipped with a thermal conductivity detector and a flame ionization detector (FID). The conversion was determined by the differences between the inlet and outlet concentrations. For C₃H₈ oxidation, the products almost completely belong to CO₂. And the CO₂ concentration was measured by FID (before detection, it was converted to CH₄ by a Ni-based catalyst mounted in a furnace), leading to a well-matched carbon balance.

3. Results

3.1. Textural and structural properties by physical characterization

The nitrogen adsorption/desorption isotherms and the corresponding BJH pore size distributions of the catalysts are shown in Fig. 1. It can be seen that the isotherms of all the catalysts exhibit typical IV shape, with the P/P₀ position of the inflection point corresponding to a diameter in the mesoporous range. The hysteresis loops belong to the H₂ type, suggesting that the mesopores are randomly distributed, possibly formed by the surfactant-assisted nanoparticles assembly [21]. The pore diameters are narrowly centered ranging from 4 to 8 nm, indicating that these oxides possess mesoporous structure in good homo-

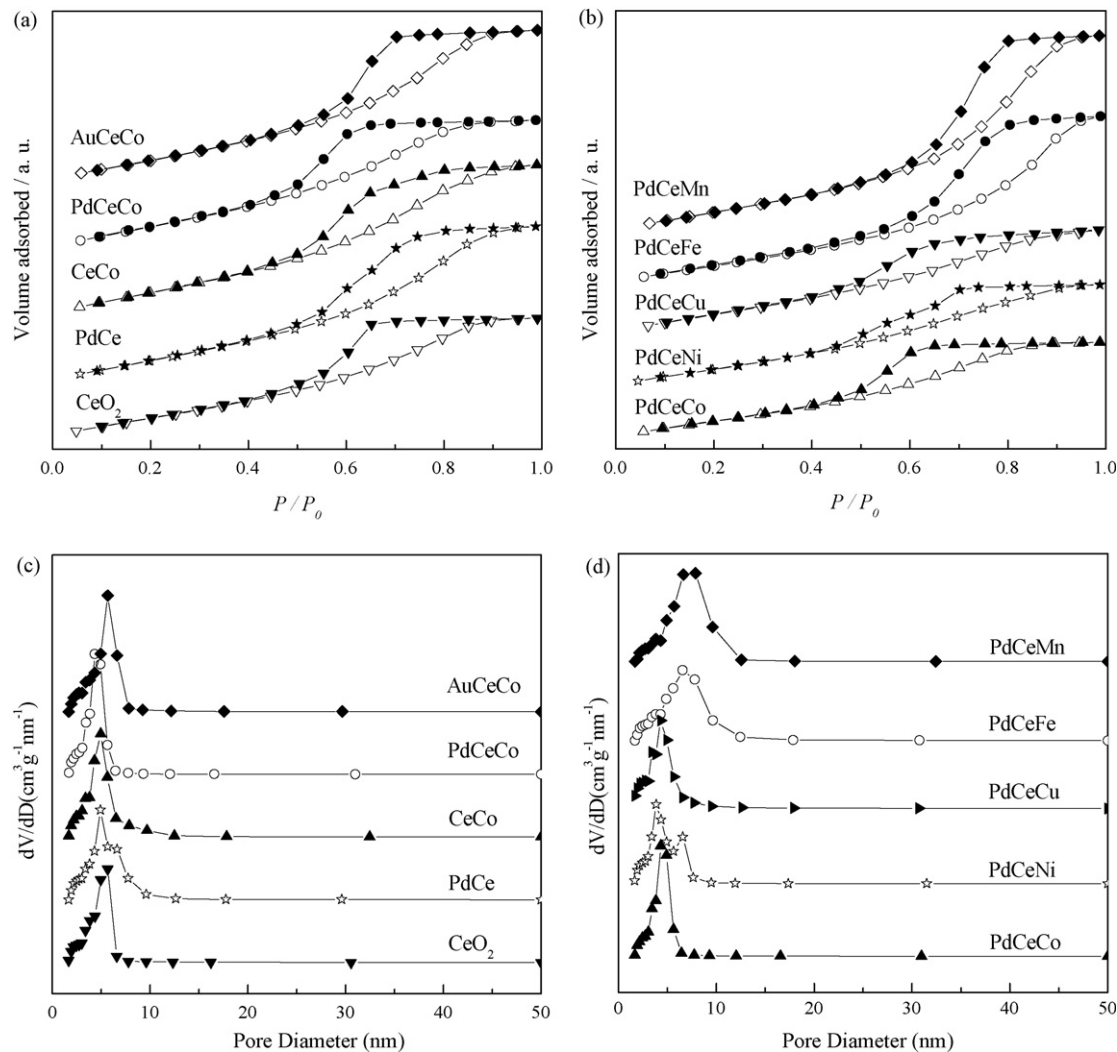


Fig. 1. Nitrogen adsorption/desorption isotherms (a, b) and BJH pore size distribution of the oxides (c, d).

geneity. The textual properties of the mixed oxides are summarized in Table 1. All the mixed oxides exhibit high specific surface area exceeding $115 \text{ m}^2 \text{ g}^{-1}$. Among them, the PdCeMn possesses the largest surface area up to $144 \text{ m}^2 \text{ g}^{-1}$. Meanwhile, it is worth noting that the PdCeCo shows much larger surface area than the impregnated sample ($118 \text{ m}^2 \text{ g}^{-1}$ vs $85 \text{ m}^2 \text{ g}^{-1}$) [17].

XRD patterns of the samples are shown in Fig. 2. The principal reflections seen in the diffraction patterns can be ascribed to fluorite CeO₂. The mean CeO₂ crystallite sizes of the mixed oxides,

determined with Scherrer equation, are shown in Table 1. The CeO₂ crystallites in the 3d-transition metal-containing oxides are all in the range of ca. 4–6 nm, smaller than pure CeO₂ and PdCe sample. Among them, the PdCeMn has the smallest CeO₂ size of only 3.9 nm.

For the cobalt-containing samples as shown in Fig. 2a, some peaks at 43 and 77.6° , typical of spinel Co₃O₄, are clearly visible. The average Co₃O₄ crystallite sizes were not determined from the diffraction peaks, however, due to their weak characters. After

Table 1
Texture data and crystallite size of CeO₂ in the catalysts

Sample	$S_{\text{BET}} (\text{m}^2 \text{ g}^{-1})$	Pore diameter (nm)	Pore volume ($\text{cm}^3 \text{ g}^{-1}$)	Crystallite size (nm) ^a	Noble metal content (wt%) ^b
CeO ₂	104	5.7	0.141	8.4	–
CeCo	121	4.9	0.175	6.0	–
PdCe	119	4.9	0.180	7.8	0.43
AuCeCo	116	5.7	0.174	6.0	0.45
PtCeCo	119	4.9	0.197	5.9	0.46
PdCeCo	118	4.3	0.156	5.8	0.45
PdCeMn	144	7.9	0.290	3.9	0.45
PdCeFe	132	6.6	0.241	6.1	0.45
PdCeNi	124	3.9	0.163	5.5	0.45
PdCeCu	137	4.3	0.166	5.2	0.47

^a Estimated from the line broadening of the (1 1 1) reflection of CeO₂ using Scherrer equation.

^b Measured by AAS.

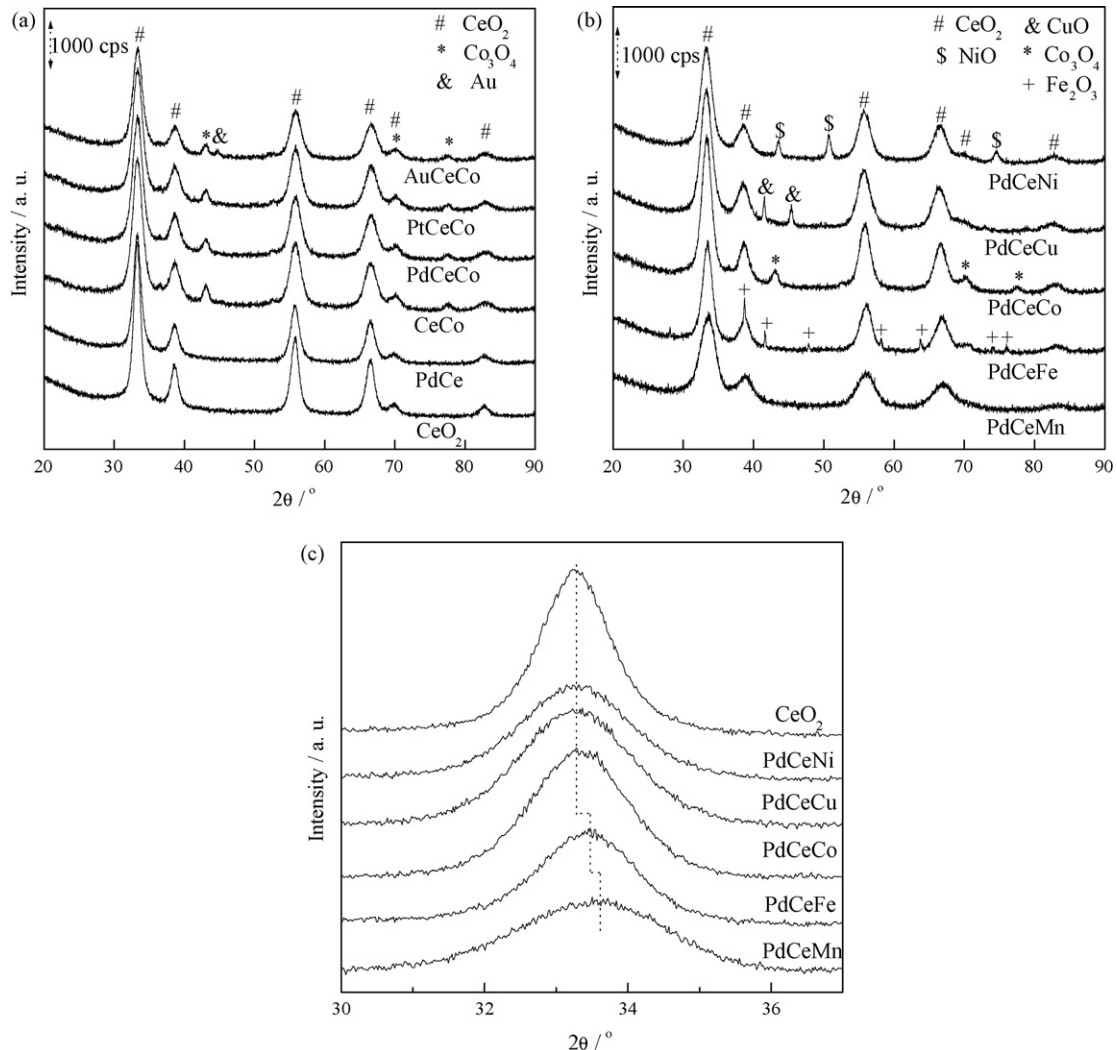


Fig. 2. XRD patterns of the catalysts. (a) CeO_2 , PdCe and cobalt-related oxides; (b) and PdCeM ; (c) enlarged (1 1 1) reflections of CeO_2 .

promotion of the oxide Co_3O_4 - CeO_2 with small amount of Pt, Pd or Au, no peaks related to Pt or Pd can be detected, suggestive of their high dispersion state; however, the main diffraction peak of Au can be identified at 44.7° despite its low loading, which is possibly due to the sintering of Au. With respect to the PdCeM catalysts as shown in Fig. 2b, corresponding diffraction peaks of MO_x , such as NiO , CuO , Co_3O_4 and Fe_2O_3 , can be clearly detected except PdCeMn .

In literature [22], three kinds of Mn species were reported for the MnO_x - CeO_2 catalysts prepared by CA method, namely aggregated Mn_2O_3 on the CeO_2 support, highly dispersed Mn_2O_3 with strong interactions with CeO_2 , and Mn atoms incorporated into the CeO_2 lattice. Since no aggregated MnO_x can be detected in the PdCeMn catalyst, it is very likely that MnO_x is highly dispersed on the CeO_2 support or even incorporated into the CeO_2 lattice. For figuring out this, the diffraction peaks of PdCeM corresponding to CeO_2 crystal plane (1 1 1) were enlarged and shown in Fig. 2c. It can be clearly seen that this peak of PdCeMn shifts to higher values as compared to pure CeO_2 , suggesting that the Mn atoms are incorporated into CeO_2 lattice, with the formation of a MnO_x - CeO_2 solution. The formation of such solid solution is due to the structural similarity between Mn_2O_3 and CeO_2 . The crystal structure of Mn_2O_3 is the C-rare earth type that is basically composed of anion-deficient units of fluorite structure [22]. Since Mn^{3+} (ionic radius: 0.66 Å) is smaller than Ce^{4+} (ionic radius:

0.92 Å), the replacement of Ce^{4+} by Mn^{3+} will result in the contraction of the unit cell, as well as the consequent shift of the 2θ to higher value. It is worth noting that there is also a small incremental shift of this diffraction for the PdCeFe catalyst, but to a less extent as compared with PdCeMn , suggesting that part of the Fe^{3+} is also incorporated into the CeO_2 lattice. The solid solution between Fe_2O_3 and CeO_2 has also been reported in literature [23,24].

TEM and HR-TEM images of some typical catalysts are shown in Fig. 3. All catalysts exhibit aggregated nanoparticles with small and uniform sizes. No well-defined structure like in the Si-containing molecular sieves was observed, suggesting that the mesopores with uniform size are randomly distributed between nanoparticles, consistent with the BET results. HR-TEM images indicate that these particles are mainly CeO_2 crystallites, exposing preferentially the crystal plane (1 1 1). Meanwhile, the CeO_2 crystallites display nearly the same sizes as that obtained by XRD calculations, and it is very clear that this size is smaller in PdCeMn than in PdCeCo .

The chemical state and relative proportion of the elements on the surface of the catalysts PdCeM were studied by XPS technique. The Pd 3d and Ce 3d core levels of the PdCeM catalysts are displayed in Fig. 4, while the relative M/(M + Ce) ratios are summarized in Table 2. Very low concentration of palladium (surface atomic ratio: $\approx 0.1\%$) is present on the surface. According

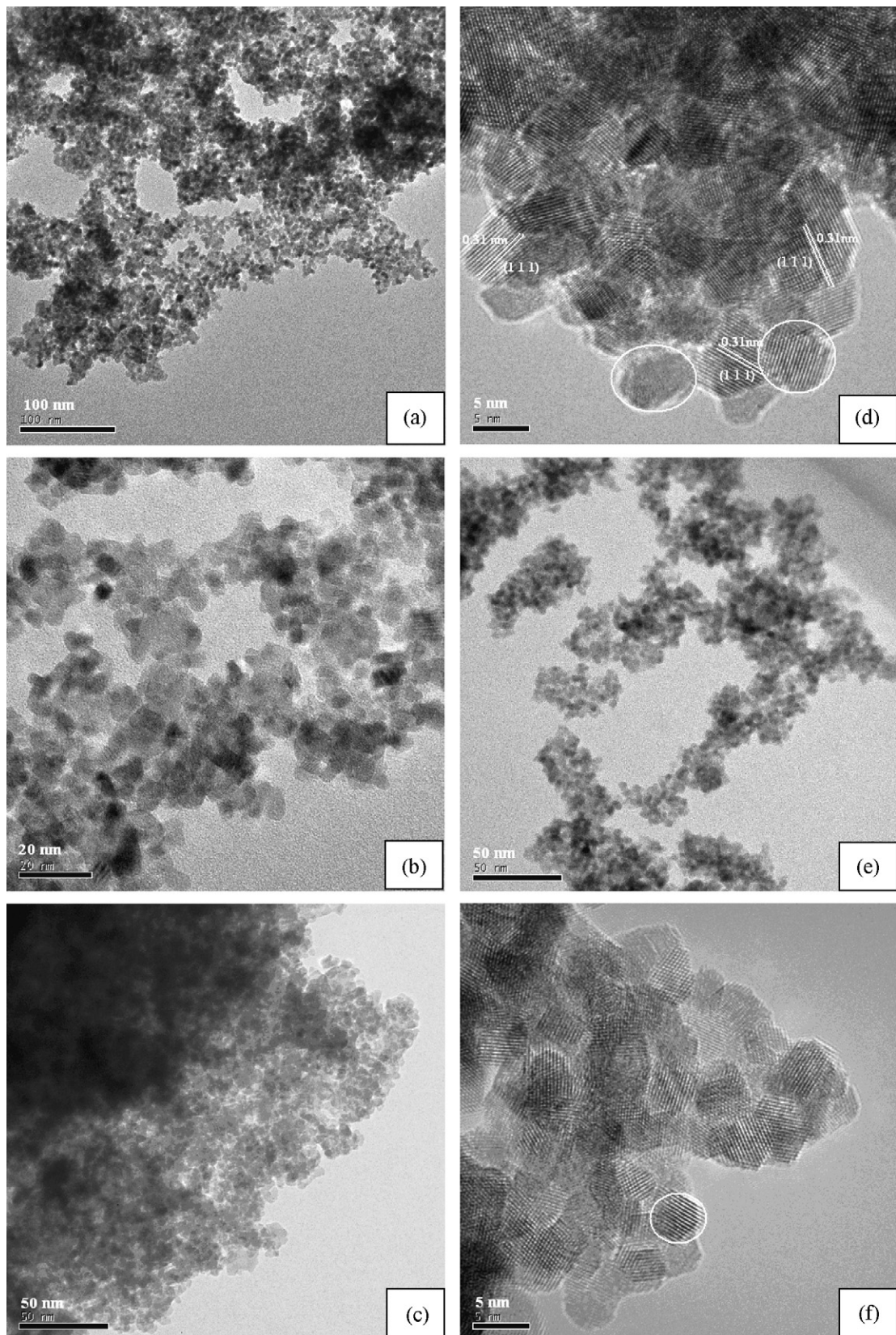


Fig. 3. TEM and HR-TEM images of the catalysts. (a, b) PtCeCo; (c, d) PdCeCo; (e, f) PdCeMn.

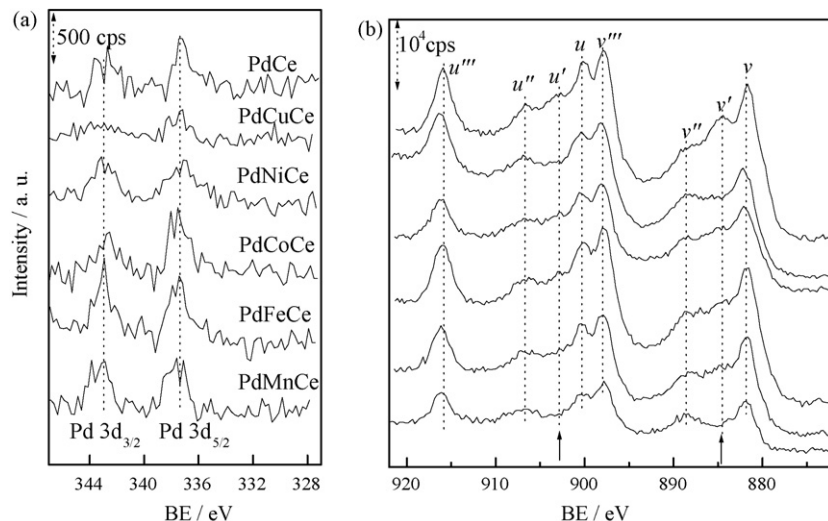


Fig. 4. XPS spectra of the catalysts. (a) Pd 3d; (b) Ce 3d.

to the binding energy of Pd 3d_{5/2} at 337.3 eV (336.8 eV in PdO and 338.3 eV in PdO₂) [25], the palladium is oxidized, likely as a mixture PdO and PdO₂. Meanwhile, the platinum in PtCeCo is also oxidized, with the binding energy at 72.7 and 76.0 eV corresponding to PtO [26]. The Au in AuCeCo is present in metallic state, consistent with the XRD results. With respect to the transition metals, their XPS spectra correspond to the species already identified by XRD technique, such as NiO, CuO, Fe₂O₃, and Co₃O₄. For PdCeMn, it is found that Mn is present as Mn³⁺, with the Mn 2p_{3/2} binding energies at 641.3 eV [27]. Regarding Ce 3d spectra, eight peaks, labeled as *u* (*u*-*u''*) for 3d_{3/2} and *v* (*v*-*v'''*) for 3d_{5/2}, are displayed in Fig. 4. Among them, the doublet (*v'*, *u'*) is considered as the character of Ce³⁺ whereas the others as Ce⁴⁺ [28]. It can be seen that the transition metals have great influence on the electronic properties on the surface CeO₂. The catalyst PdCeMn exhibits extremely low surface concentration of Ce³⁺, and the other catalysts exhibit the presence of Ce³⁺ clearly, particularly in PdCeCo and PdCeNi catalysts, while the catalyst PdCe without MO_x shows the largest portions of Ce³⁺. Generally, when Ce⁴⁺ ions are substituted by Mn³⁺ ions, oxygen vacancies must be generated for charge balance, resulting in high concentration of Ce³⁺. Contrary to this, the concentration of Ce³⁺ in PdCeMn is very low, suggesting the presence of another kind of Mn ions, namely interstitial Mn³⁺ sites, in the fluorite lattice. In this case, the interstitial oxygen species can diffuse to adjacent oxygen vacancies associated with Mn³⁺ at the Ce⁴⁺ sites, leading to low concentration of oxygen vacancies. Similarly, due to the presence of the interstitial sites, the low concentrations of Ce³⁺ have been observed in the Ce_{1-x}Fe_xO₂ solid solutions prepared by a hydrothermal method [23].

Table 2
XPS results and CO oxidation activity of the catalysts

Sample	M/(M + Ce) ^a	M/(M + Ce) ^b	T ₅₀ (°C) ^c	T ₅₀ (°C) ^d	ΔT (°C) ^e
PdCeMn	0.273	0.50	<40	111	>71
PdCeFe	0.320	0.36	65	179	114
PdCeCo	0.274	0.10	70	112	42
PdCeNi	0.283	0.18	99	123	24
PdCeCu	0.308	0.31	66	62	-4

^a Volume content measured by AAS.

^b Surface ratio measured by XPS.

^c Light-off temperatures of the PdCeM.

^d Light-off temperatures of the CeM.

^e Differences between superscripts c and d.

The surface M/(M+Ce) ratios are shown in Table 2. Compared with the bulk composition as determined by AAS, a surface enrichment of Mn and Fe elements, and a surface deficiency of Ni and Co can be observed in the corresponding PdCeM catalysts. During the previous preparation of Co₃O₄-CeO₂ catalysts, it was found that the preparation method can generate precursors with a CeO₂-covered encapsulation structure [17]. Therefore, after calcination, the resultant catalysts are enriched with ceria on the surface, like in PdCeCo and PdCeNi catalysts here, or in the reported Mn-Ce-O composites calcined at low temperature 350 °C [29]. Here the surface enrichment of Mn and Fe is possibly related to their high mobility during calcination at relatively high temperature of 500 °C. The solubility of Mn and Fe ions in CeO₂ lattice possibly promotes their migration to the surface during calcination because of the decreased diffusion resistance.

3.2. Redox properties

The H₂-TPR profiles of CeO₂, PdCe and cobalt-related catalysts are displayed in Fig. 5a. Pure CeO₂ exhibits two reduction peaks, one at about 500 °C and the other at 820 °C, attributed to the reduction of surface capping oxygen and bulk oxygen species, respectively. After doping with small amount of Pd, the surface reduction is greatly promoted, as indicated by the sharp reduction peak at 180 °C, possibly due to the hydrogen spillover effect. Concerning the reduction pattern of CeCo, two main reduction peaks can be observed, one at 293 °C and the other at 560 °C, due to the two-step reduction of Co₃O₄ involving CoO intermediate. Similarly, after doping with precious metals, both reduction steps are promoted due to the hydrogen spillover effect, but to a different extent depending on the types of metals. The degree of promotion increases in the order of Au < Pt < Pd. It is worth noting that Co₃O₄ in PdCeCo is reduced at lower temperature than that in impregnated Pd/CeCo catalyst (first reduction peak at 154 °C) [17], indicative of the more enhanced interaction between Pd and Co₃O₄ in the co-precipitated sample.

Using the H₂ consumption of known amounts of CuO as reference, we quantitatively calculated the hydrogen consumption of the CeCo-related samples. It is found that below 600 °C, the hydrogen consumption is about 1.25 times larger than those required for the reduction of Co₃O₄ to Co. Therefore, considerable amount of CeO₂ is also reduced. It is calculated that about 0.106 mol H₂ is consumed per mol CeO₂, close to the value 0.10 in

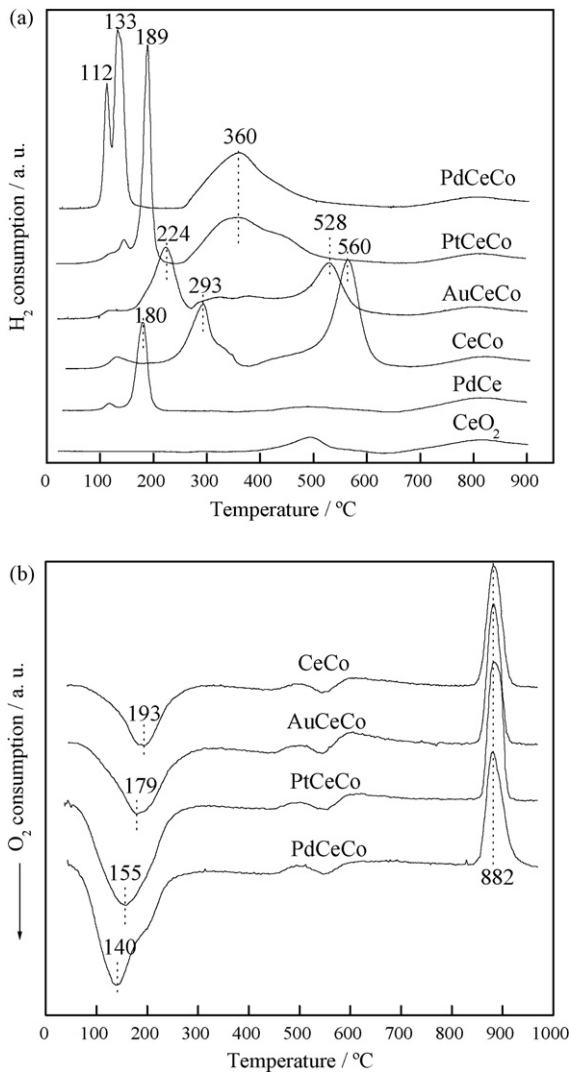


Fig. 5. H_2 -TPR (a) and TPO (b) profiles of the Co-related catalysts.

the sample PdCe. Moreover, it is found that the excess hydrogen is mainly consumed during the first reduction step of Co_3O_4 , which means that the CeO_2 is reduced simultaneously with the reduction of Co_3O_4 to CoO , which is due to the metal–support strong interaction that promotes the reduction of ceria.

The TPO profiles of the cobalt-related catalysts are displayed in Fig. 5b. Two peaks can be identified, namely a low-temperature oxygen consumption peak related to the oxidation of the cobalt species, and an oxygen evolution peak at constant temperature 880 °C due to the thermal decomposition of Co_3O_4 into CoO [30]. Doping with precious metals promotes the oxidation of cobalt species, and the degree of promotion increases in the order of $Au < Pt < Pd$. Similar to H_2 -TPR, such a promotion can be attributed to oxygen spillover since these precious metals possess strong oxygen activation ability.

As a result of the spillover effect, it is hard to differentiate from H_2 -TPR whether the Co–O bond length is modified after precious metals promotion. But the hydrogen spillover effect can be eliminated in CO-TPR. Therefore, CO-TPR is tested and the profiles are displayed in Fig. 6. For the catalyst CeCo, the relatively small peak at 253 °C can be attributed to the reduction of surface Co_3O_4 whereas the wide reduction peak between 300 and 700 °C is related to the reduction of bulk Co_3O_4 since the CO-TPR involves in

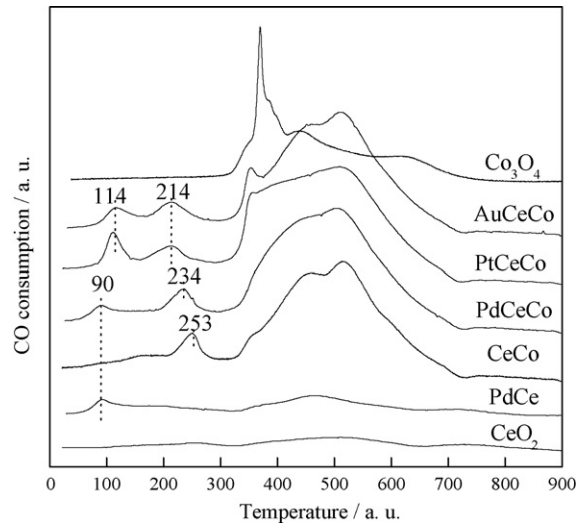


Fig. 6. CO-TPR profiles of the Co-related catalysts.

a surface-to-bulk reduction property [26]. After doping with precious metals, the reduction of surface Co_3O_4 is promoted, as indicated by the decreased peaks at 234 °C for PdCeCo, and 214 °C for PtCeCo and AuCeCo. This is different from the impregnated Pd/CeCo catalyst where the reduction of surface Co_3O_4 is almost unchanged [17]. In the low-temperature range, small peaks can be also observed at 90 °C for PdCeCo, and 114 °C for PtCeCo and AuCeCo, which is related to the reduction of the precious metal oxides and/or the boundaries between precious metal and ceria.

The H_2 -TPR profiles of the PdCeM catalysts and the corresponding CeM catalysts are displayed in Fig. 7a and b, respectively. For CeM oxides, two main peaks can be observed. With respect to CeCu and CeNi catalysts, these two peaks can be attributed to the reduction of the transition metal oxides that strongly and weakly interacted with CeO_2 [31,32], whereas for the CeCo, CeFe and CeMn catalysts, these two peaks are related to the stepwise reduction of the transition metal oxides, involving in CoO , Fe_3O_4 and Mn_3O_4 intermediates [33,34]. Among them, the CeCu catalyst is most reducible, and the CeFe catalyst least reducible. Their first reduction peak stands at 185 and 412 °C, respectively, whereas the first reduction peaks of the other three CeMn, CeCo and CeNi catalysts are almost in the same temperature range. After doping with Pd, as shown in Fig. 7a, nearly all the reduction of these catalysts is greatly promoted as a result of hydrogen spillover effect. It is worth noting that although the reduction of the bulk-like CuO that weakly interacted with CeO_2 is greatly promoted, the reduction of highly dispersed CuO species that strongly interacted with CeO_2 is almost unchanged. Due to the strong interaction between them, these dispersed CuO species can already get reduced easily at very low temperature, which makes the effect of Pd unobvious.

3.3. Catalytic performance for CO and C_3H_8 oxidation

The catalytic performance for CO and C_3H_8 oxidation over these catalysts is illustrated in Fig. 8. For CO oxidation, it can be seen that Pt and Au doping just slightly improves the activity of the CeCo, whereas Pd doping greatly improves its activity, decreasing the T_{50} from 112 to 70 °C. Moreover, the activity of PdCeCo is also much higher than that of PdCe, suggesting that there exists a synergism between Pd and Co_3O_4 , similar to that in the impregnated Pd/CeCo. For these PdCeM catalysts as shown in Fig. 8a, the activities are in the order of $PdCeMn > PdCeCu = PdCeFe > PdCeCo > PdCeNi$. The

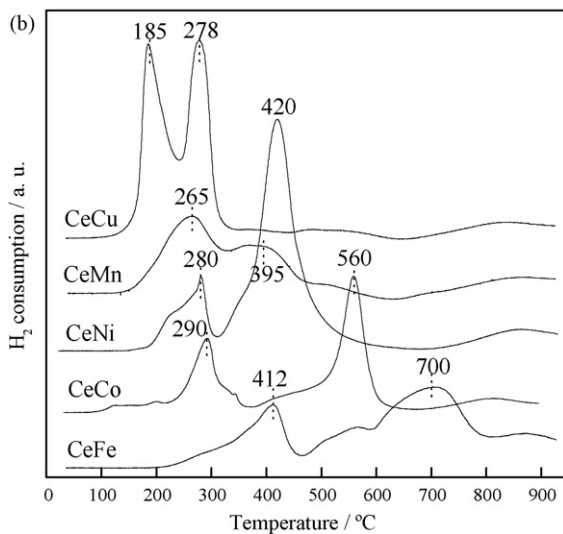
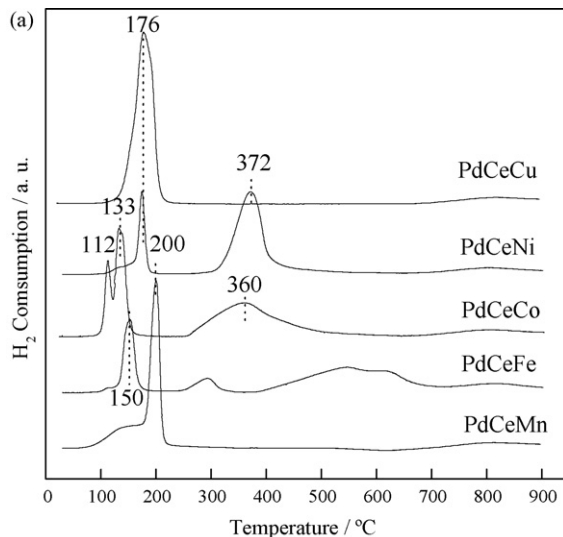


Fig. 7. H₂-TPR profiles of the catalysts. (a) PdCeM; (b) CeM.

PdCeMn exhibits excellent CO oxidation activity, and an 80% conversion can be achieved even at room temperature. Meanwhile, the PdCeFe, PdCeCu and PdCeCo catalysts show high activity as well, and CO can be completely oxidized at temperatures lower than 100 °C.

From Fig. 8b, it can be seen that Pd or Au doping can hardly modify the catalytic activity of the CeCo towards C₃H₈ oxidation, and Pt doping just slightly promotes its activity. Among the PdCeM catalysts, the C₃H₈ oxidation activities are in the order of PdCeCo > PdCeMn > PdCeNi > PdCeCu > PdCeFe > PdCe. The PdCeCo and PdCeMn catalysts exhibit excellent catalytic oxidation activity, and C₃H₈ can be totally oxidized over these catalysts below 300 °C.

Concerning CO and C₃H₈ oxidation, the PdCeCo and PdCeMn catalysts show the best activity. Their time-on-line activities are tested and shown in Fig. 9. It can be seen that both catalysts exhibit very stable activity for C₃H₈ oxidation. For CO oxidation over fresh PdCeMn catalyst, a slow deactivation can be observed with increasing reaction time, which is possibly due to the accumulation of H₂O and/or carbonates on the catalyst surface at relatively low temperatures. However, following C₃H₈ oxidation at 280 °C as shown in curve (3) and flushing with 5% O₂/N₂, its high CO

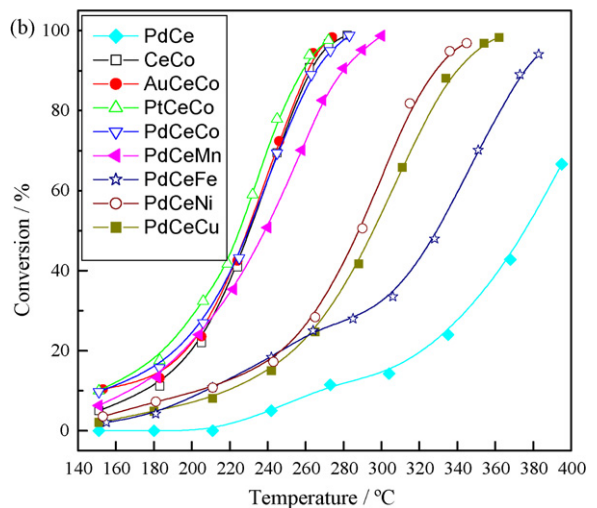
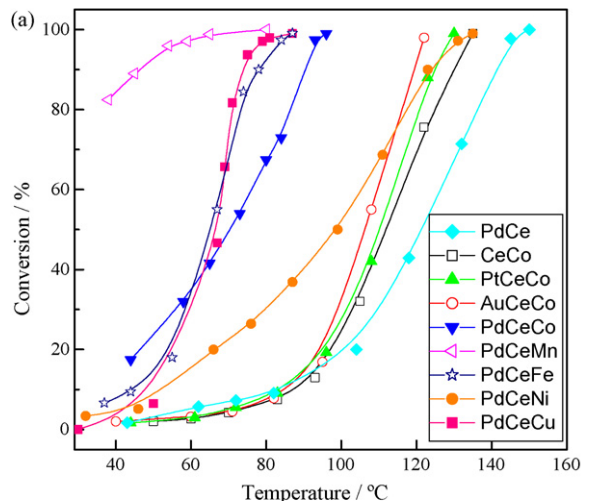


Fig. 8. Catalytic performance of the catalysts for (a) CO and (b) C₃H₈ oxidation.

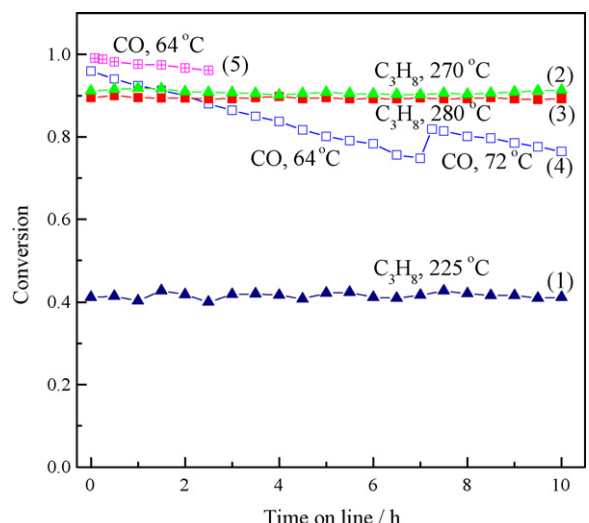


Fig. 9. Stability test of the catalyst PdCeCo and PdCeMn. C₃H₈ oxidation over PdCeCo (1) (2) and PdCeMn (3); CO oxidation over fresh PdCeMn (4) and used PdCeMn (5). Reaction conditions are detailed in text.

oxidation activity can be completely recovered, as indicated in curve (5). For the used PdCeMn catalyst, the results of XPS measurements show that no obvious change occurs to the surface state of the catalyst.

4. Discussion

In this work, the precious metal-promoted $\text{MO}_x\text{-CeO}_2$ mixed oxides were synthesized in one step. The precious metals were selected from Pt, Pd and Au, and the transition metals from Mn, Fe, Co, Ni and Cu. The aim of the present study was to investigate the reaction mechanisms for CO and C_3H_8 oxidation from a broad point of view, in order to develop highly active and low-cost catalyst for the abatement of hazardous emissions during the cold start.

4.1. Effect of precious metals

For CO oxidation, the Pd-doped CeCo is much more active than the Pt- or Au-doped CeCo, which seems to be consistent with the H₂-TPR and TPO results since the cobalt species in PdCeCo are more easily reduced and oxidized. However, the CO-TPR results

show that the surface Co_3O_4 of PtCeCo and AuCeCo seems to be more easily reduced than that of PdCeCo, which is not in the same sequence as the oxidation activity. Therefore, the CO oxidation activity cannot be simply correlated with the surface state of cobalt species, like the mobility of the Co–O bond, but more probably determined by the synergy between the precious metals and Co_3O_4 . Although Au is reported to be a very active catalyst for CO oxidation [35], it is suggested by XRD that Au is sintered after calcination at relatively high temperature of 500 °C. Meanwhile, The CO-TPR indicates that PdO_x is more easily reduced than PtO_x . On this basis, we conclude that in comparison with Pt or Au, the higher reducibility, the higher thermal resistance and the higher amount of active sites per mass of additive, make Pd be a more efficient additive for CO oxidation. Therefore, Pd is chosen as additive for other $\text{MO}_x\text{-CeO}_2$ catalysts.

Although there is a synergy between even a small amount of Pd and Co_3O_4 for CO oxidation, such effect does not exist in the process of C_3H_8 oxidation. Only the Pt-doped CeCo catalyst shows slightly higher activity which can not be called synergy. Such discrepancies are mainly attributed to their different reaction mechanisms or rate-determining steps, so, we discuss them carefully in the following sections.

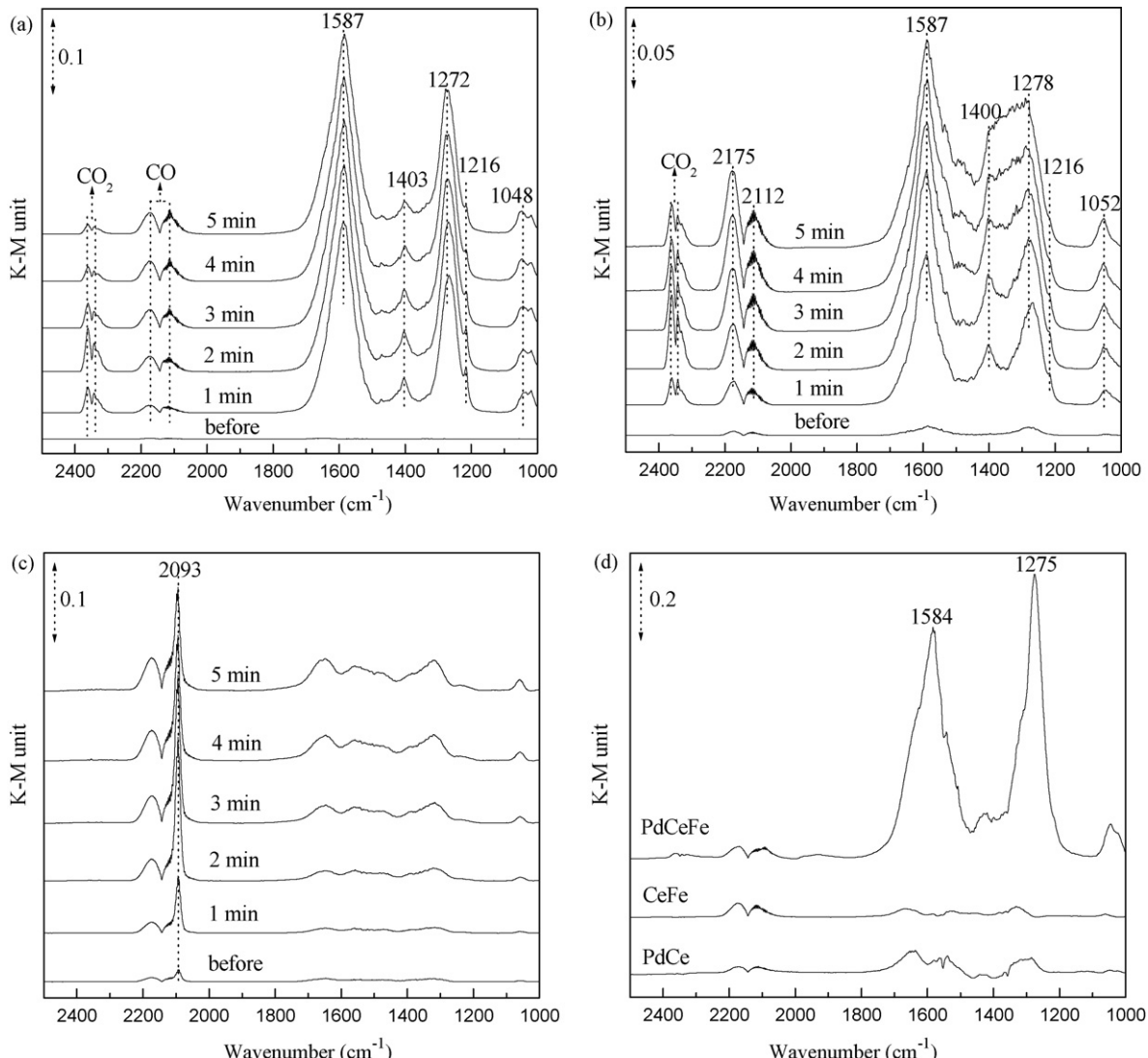


Fig. 10. DRIFTS spectra after exposure the catalyst (a) PdCeMn, (b) PdCeCo, and (c) PdCeCu to CO/O_2 at room temperature in 5 min; (d) the comparative spectra of the PdCe, CeFe and PdCeFe after exposure to CO/O_2 for 5 min.

4.2. Synergistic effects between Pd and 3d-transition metal oxides for CO oxidation

There is a synergistic effect between Pd and Co_3O_4 on CO oxidation. In order to probe the extent of synergism between Pd and other 3d-transition metal oxides, CeM catalysts without precious metal doping were also prepared. Their CO oxidation activities were determined for the purpose of comparison, and the light-off temperatures are listed in Table 2. Among them, the CeCu catalyst is most active while the CeFe catalyst is least active, with the T_{50} of 62 and 179 °C, respectively. The other three catalysts CeMn, CeCo and CeNi exhibit similar activities with the T_{50} between 110 and 120 °C. The catalytic performance of the catalysts is well-correlated with the TPR results, namely the lower reduction temperature corresponds to the higher activity. After Pd doping, the activities are generally promoted, but it seems that no correlation exist between the reducibility and the activity of the catalysts. On the other hand, the surface concentration of Ce^{3+} , an indication of the oxygen vacancies, cannot be related to the oxidation activity, either. Therefore, DRIFTS studies were then performed, in order to gain some information about the reaction mechanisms.

Fig. 10a exhibits the spectra of CO/O_2 co-adsorption over the PdCeCo at room temperature. The most predominant feature is the appearance of very strong bands at 1587 and 1272 cm^{-1} due to bidentate carbonate species, besides some bands of gaseous CO and CO_2 . Meanwhile, these bidentate carbonate species can be also identified in PdCeMn, PdCeFe and PdCeNi samples. On this basis, we conclude that CO oxidation over these catalysts possibly occurs via bidentate carbonate intermediate, in agreement with the previous findings in the Pd/ Co_3O_4 - CeO_2 prepared by impregnation and the Ir-in- CeO_2 [17,20]. Interestingly, for CO/O_2 co-adsorption over the PdCeCu, as shown in Fig. 10c, bands of carbonates are relatively rather weak, whereas strong carbonyl band at 2093 cm^{-1} due to CO adsorbed over Cu^+ is observed [36]. It is very probable that CO oxidation over PdCeCu proceeds via a carbonyl intermediate, but not the bidentate carbonate species.

As shown in Table 2, the CeFe catalyst is very inactive, with the T_{50} at 179 °C, whereas the Pd doping greatly promotes its activity, decreasing the T_{50} by 114 °C. Therefore, we chose the PdCeFe system for further investigation, in order to figure out the synergistic essential between them. The comparative DRIFTS spectra of PdCe, CeFe and PdCeFe after CO/O_2 co-adsorption for 5 min were measured and displayed in Fig. 10d. It can be seen that only trace amounts of carbonate species are formed over the CeFe and PdCe, whereas large amounts of bidentate carbonate species are formed over the PdCeFe. From this, it can be expected very active oxygen species are generated in PdCeFe, which are not present in PdCe and CeFe, possibly due to the interaction between Pd and Fe_2O_3 . Such species react readily with adsorbed CO, forming the reaction intermediates, mainly the bidentate carbonate species. Previously, it was thought that the oxygen activation takes place only on Pd sites over the Pd/ Co_3O_4 - CeO_2 system [17]. From the PdCeFe system here, it seems that the interaction between Pd and transition metal oxides also plays a crucial role for oxygen activation. In an Au/ MnO_x /C catalyst, it has been proposed that the oxygen is activated at the interface between Au and MnO_x , similar to our findings [37]. Using molecular beam method and high-resolution photoelectron spectroscopy, an active oxygen layer has been identified at the particle/support interface in a model Pd/ Fe_3O_4 catalyst [38]. On this basis, it can be deduced that the interaction between Pd and 3d-transition metal oxides can facilitate the activation of gas phase oxygen, with the formation of active oxygen species. Since the oxygen activation is generally regarded as the rate-determin-

ing step for CO oxidation at low temperatures, the synergistic essential here can be expressed as the interaction-assisted oxygen activation. The TPO results indicate that the activated oxygen species can spill over on the catalyst surface, therefore, even a small amount of Pd doping can greatly enhance the CO oxidation reaction.

In order to figure out the extent of the synergism between Pd and MO_x , the T_{50} differences before and after Pd loading were calculated and listed in Table 2. It can be seen that CO oxidation over different catalysts is affected differently by Pd doping, depending on the types of 3d-transition metals. The activity of CeMn and CeFe is promoted to the largest extent, with the T_{50} decreased by more than 70 and 100 °C, respectively. Meanwhile, the catalytic activity of CeCo and CeNi is promoted as well, but to a less extent. However, no promotion can be observed for CeCu. According to the XRD and XPS measurements, a solid solution between $\text{Mn}_2\text{O}_3/\text{Fe}_2\text{O}_3$ and CeO_2 is formed in the PdCeMn and PdCeFe catalysts. From another point of view, it can be considered that parts of Mn and Fe ions are dispersed throughout CeO_2 on an atomic scale. In this case, very strong interaction between Pd and these oxides can be expected, possibly via direct contact, resulting in greatly enhanced activity. Whereas a decreased interaction can be expected in other catalysts, and the synergism between Pd and the MO_x is relatively weaker. It is worth noting that no enhancement is observed for the Pd-promoted CeCu. In literature, it is well documented that the CuO- CeO_2 catalyst exhibits remarkable activity for CO oxidation. TPR results show that the CuO species interacting with CeO_2 can be easily reduced at very low temperature, which is almost independent of the presence of Pd. Moreover, oxygen can be readily dissociated on interaction with the reduced species even at 77 °C [39]. All these factors make the effect of Pd unobvious.

4.3. Effect of 3d-transition metals on C_3H_8 oxidation

In literature, the propane oxidation activities are reported to be related to the reducibility for the MnCu mixed oxides [40], or the existence of oxygen vacancies for oxygen activation and transportation for the Ca-substituted LaCoO₃ perovskites [41]. Concerning the mixed oxides here, it is found that their CO oxidation performance is related to their reducibility for the CeM catalysts, and oxygen activation ability for the PdCeMn catalysts, however, their C_3H_8 oxidation activity cannot be simply related to these properties, which strongly suggests that the reaction mechanisms for CO and C_3H_8 oxidation are quite different over these catalysts. Such differences have also been identified by the comparison between CuO- CeO_2 and Co_3O_4 - CeO_2 catalysts [42], as well as in the oxide-supported gold catalysts [43]. Regarding C_3H_8 oxidation, it takes place at much higher temperatures than CO oxidation, so the oxygen activation may be not a rate-limiting step any more. It has been reported that the light-off temperatures of the saturated hydrocarbons oxidation are closely related to the strength of C-H bond [44]; therefore, it is very likely that the C-H bond activation in C_3H_8 molecule determines the reaction rate. The different catalytic activities of the PdCeM catalysts are related to the C-H activation ability of the 3d-transition metal oxides.

Generally, it is rather difficult to directly measure the C-H activation ability over these metal oxides. However, we think that the C-H activation ability here can be reflected by another kind of redox properties, denoted as TOF_{redox}, which was first proposed by Badlani and Wachs [45]. Using methanol as probe molecule, the TOF_{redox} values of a large number of oxides at 300 °C are determined by them, according to the product distribution. It is considered that TOF_{redox} is dependent on the rate-determining surface decomposition of the surface methoxy intermediate that

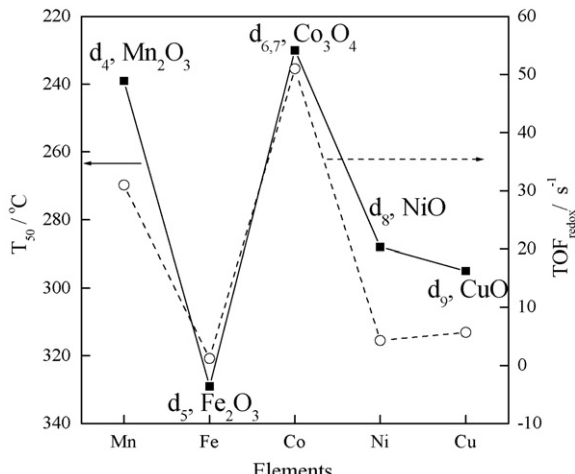


Fig. 11. Plots of light-off temperature T_{50} for propane oxidation over PdCeM catalysts vs $\text{TOF}_{\text{redox}}$ of the corresponding 3d-transition metal oxides. $\text{TOF}_{\text{redox}}$ from Ref. [45] using methanol oxidation test reaction.

involves the breaking of C–H bond. In Fig. 11, the light-off temperature T_{50} for C_3H_8 oxidation and the $\text{TOF}_{\text{redox}}$ of the corresponding 3d-transition metal oxides are presented. It can be seen that they are well-correlated, indicating that the C–H bond activation really consists of the rate-determining step in propane oxidation. In addition, it is worth noting that the $\text{TOF}_{\text{redox}}$ of PtO is extraordinarily large, up to 9143 s^{-1} , which is hundreds of times larger than those of the 3d-transition metal oxides and PdO, suggesting the high capability of Pt in breaking C–H bond. Therefore, Pt-based catalysts generally show excellent activity for saturated hydrocarbon oxidation [46], and it is natural that the trace amounts of exposed Pt on the surface of $\text{Co}_3\text{O}_4\text{-CeO}_2$ can slightly promote the C_3H_8 oxidation activity.

The question remaining is that, what is the intrinsic reason for the differences in their C–H breaking ability for these 3d-transition metal oxides. We believe that the electronic structure of the d-type orbitals plays a crucial role, since it has been proposed by Finocchio et al. that C–H bond breaking on metal oxides firstly occurs via direct interaction (or couple of electrons) of σ and σ^* C–H orbitals with d-type orbitals of transition metal cations [47]. Generally, the transition metal cations with d_0 , d_5 and d_{10} electronic configurations are very stable (crystal field stabilization energy (CFSE) is very low), leading to their low oxidation activities, such as for TiO_2 , Fe_2O_3 , and ZnO ($\text{TOF}_{\text{redox}}$ value: 0, 1.2, and 2). On this basis, with respect to the 3d-transition metal oxides as shown in Fig. 11, a ‘double-peak’ behavior for propane oxidation can be expected with increasing the number of the d-electrons. Actually, such a phenomenon can be also observed in the perovskite-type oxides, RMO_3 (R = lanthanides, M = Cr, Mn, Fe, Co, Ni) for propane oxidation at $500 \text{ }^{\circ}\text{C}$ [48]. The d_4 and $\text{d}_{6,7}$ character with high CFSE may facilitate the electronic interaction with C–H bond, and contribute to the excellent propane oxidation activity of Mn_2O_3 and Co_3O_4 .

5. Conclusion

A series of nanostructured precious Pd-doped mixed oxides $\text{MO}_x\text{-CeO}_2$ (M = Mn, Fe, Co, Ni and Cu) were prepared using one-step co-precipitation in the presence of surfactant CTAB. These mixed oxides exhibit uniform mesoporous structures and large surface areas exceeding $115 \text{ m}^2 \text{ g}^{-1}$.

A synergism exists between Pd and MO_x for CO oxidation. The interaction between them can facilitate the rate-limiting step, namely the oxygen activation, and generate very active oxygen

species, promoting CO oxidation via bidentate carbonate intermediate. The promotion is especially obvious for Mn and Fe-containing samples, due to the solid solution formed between $\text{Mn}_2\text{O}_3/\text{Fe}_2\text{O}_3$ and CeO_2 that strengthens the interaction between Pd and $\text{Mn}_2\text{O}_3/\text{Fe}_2\text{O}_3$, possibly via direct contact. However, no promotion is observed for CuO-CeO_2 because this catalyst already shows excellent activity for CO oxidation via a carbonyl intermediate over Cu^+ site.

The C–H bond activation is the rate-determining step for C_3H_8 oxidation. And the C–H bond breaking ability is determined by the d-type orbitals of the 3d-transition metal cations. Therefore, the C_3H_8 oxidation can be hardly promoted by the small amount of exposed precious metals, but depends on the types of the 3d-transition metal oxides.

Considering both CO and C_3H_8 oxidation, a small amount of Pd-promoted $\text{Co}_3\text{O}_4\text{-CeO}_2$ and $\text{MnO}_x\text{-CeO}_2$ catalysts prepared by the mentioned one-step co-precipitation, has shown great potential in the abatement of hazardous emissions during cold start. Since real gaseous emissions containing hazardous substances used to be more complex, including H_2O , SO_2 and other organic compounds, further work will be crucial to know if these catalysts are promising ones if complex mixtures need to be treated.

Acknowledgements

This work is financially supported by the “863 Program” of the Ministry of Science & Technology of China (No. 2006AA06Z348) and the National Natural Science Foundation of China (No. 20676097). The authors are also grateful to the support of the Program for New Century Excellent Talents in University of China (NCET-07-0599), the Cheung Kong Scholar Program for Innovative Teams of the Ministry of Education (No. IRT0641) and the Program for Introducing Talents of Discipline to Universities of China (No. B06006).

References

- [1] R. Westerholm, A. Christensen, Å. Rosén, *Atmos. Environ.* 30 (1996) 3529.
- [2] P. Thormählen, M. Skoglundh, E. Fridell, B. Andersson, *J. Catal.* 188 (1999) 300.
- [3] T.E. Davies, T. Garcia, B. Solsona, S.H. Taylor, *Chem. Commun.* 32 (2006) 3417.
- [4] M. Fernández-García, A. Martínez-Arias, A. Iglesias-Juez, A.B. Hungria, J.A. Anderson, J.C. Conesa, J. Soria, *J. Catal.* 214 (2003) 220.
- [5] M.C. Álvarez-Galván, B. Pawelec, V.A. de la Peña O’Shea, J.L.G. Fierro, P.L. Arias, *Appl. Catal., B* 51 (2004) 83.
- [6] V.A. de la Peña O’Shea, M.C. Álvarez-Galván, J.L.G. Fierro, P.L. Arias, *Appl. Catal., B* 57 (2005) 191.
- [7] V.A. de la Peña O’Shea, M.C. Álvarez-Galván, J. Requies, V.L. Barrio, P.L. Arias, J.F. Cambra, M.B. Güemez, J.L.G. Fierro, *Catal. Commun.* 8 (2007) 1287.
- [8] Y. Bi, L. Chen, G. Lu, *J. Mol. Catal. A* 266 (2006) 173.
- [9] M. Skoglundh, B. Johansson, L. Löwendahl, K. Jansson, L. Dahl, B. Hirschauer, *Appl. Catal., B* 7 (1996) 299.
- [10] L.F. Liotta, G. Di Carlo, G. Pantaleo, A.M. Venezia, G. Deganello, E. Merlone Borla, M. Pidria, *Appl. Catal., B* 75 (2007) 182.
- [11] G.L. Chiarello, D. Ferri, J.D. Grunwaldt, L. Forni, A. Baiker, *J. Catal.* 252 (2007) 137.
- [12] M. Meng, Y.Q. Zha, J.Y. Luo, T.D. Hu, Y.N. Xie, T. Liu, J. Zhang, *Appl. Catal., A* 301 (2006) 145.
- [13] L.F. Liotta, G. Di Carlo, G. Pantaleo, G. Deganello, E. Merlone Borla, M. Pidria, *Catal. Commun.* 8 (2007) 299.
- [14] J. Lojewska, A. Kołodziej, J. Źak, J. Stoch, *Catal. Today* 105 (2005) 655.
- [15] B. Solsona, T.E. Davies, T. Garcia, I. Vázquez, A. Dejoz, S.H. Taylor, *Appl. Catal., B* 84 (2008) 176–184.
- [16] V. Shapovalov, H. Metiu, *J. Catal.* 245 (2007) 205.
- [17] J.Y. Luo, M. Meng, X. Li, X.G. Li, Y.Q. Zha, T.D. Hu, Y.N. Xie, J. Zhang, *J. Catal.* 254 (2008) 310.
- [18] C.M.Y. Yeung, K.M.K. Yu, Q.J. Fu, D. Thompsett, M.I. Petch, S.C. Tsang, *J. Am. Chem. Soc.* 127 (2005) 18010.
- [19] S. Golunski, R. Rajaram, *Cattech* 6 (2002) 30.
- [20] Y.Q. Huang, A.Q. Wang, L. Li, X.D. Wang, D.S. Su, T. Zhang, *J. Catal.* 255 (2008) 144.
- [21] J.L. Cao, Y. Wang, T.Y. Zhang, S.H. Wu, Z.Y. Yuan, *Appl. Catal., B* 78 (2007) 120.
- [22] G. Qi, R.T. Yang, *J. Phys. Chem. B* 108 (2004) 15738.
- [23] G. Li, R.L. Smith, H. Inomata, *J. Am. Chem. Soc.* 123 (2001) 11091.
- [24] F.J. Pérez-Alonso, M.L. Granados, M. Ojeda, P. Terreros, S. Rojas, T. Herranz, J.L.G. Fierro, *Chem. Mater.* 17 (2005) 2329.

- [25] I. Twagirashema, M. Engelmann-Pirez, M. Frere, L. Burylo, L. Gengembre, C. Dujardin, P. Granger, *Catal. Today* 119 (2007) 100.
- [26] Q. Fu, H. Saltsburg, M. Flytzani-Stephanopoulos, *Science* 301 (2003) 935.
- [27] M. Machida, M. Uto, D. Kurogi, T. Kijima, *Chem. Mater.* 12 (2000) 3158.
- [28] G.J. Zhang, Z.R. Shen, M. Liu, C.H. Guo, P.C. Sun, Z.Y. Yuan, B.H. Li, D.T. Ding, T.H. Chen, *J. Phys. Chem. B* 110 (2006) 25782.
- [29] H. Chen, A. Sayari, A. Adnot, F. Larachi, *Appl. Catal., B* 32 (2001) 195.
- [30] L.F. Liotta, G. Di Carlo, G. Pantaleo, A.M. Venezia, G. Deganello, *Appl. Catal., B* 66 (2006) 217.
- [31] M.F. Luo, Y.J. Zhong, X.X. Yuan, X.M. Zheng, *Appl. Catal., A* 162 (1997) 121.
- [32] Y. Li, B.C. Zhang, X.L. Tang, Y.D. Xu, W.J. Shen, *Catal. Commun.* 7 (2006) 380.
- [33] F.J. Pérez-Alonso, I. Melián-Cabrera, M.L. Granados, F. Kapteijn, J.L.G. Fierro, *J. Catal.* 239 (2006) 340.
- [34] G. Picasso, M. Gutiérrez, M.P. Pina, J. Herguido, *Chem. Eng. J.* 126 (2007) 119.
- [35] M. Valden, X. Lai, D.W. Goodman, *Science* 281 (1998) 1647.
- [36] A. Martínez-Arias, M. Fernández-García, O. Gálvez, J.M. Coronado, J.A. Anderson, J.C. Conesa, J. Soria, G. Munuera, *J. Catal.* 195 (2000) 207.
- [37] Z. Ma, C.D. Liang, S.H. Overbury, S. Dai, *J. Catal.* 252 (2007) 119.
- [38] T. Schalow, M. Laurin, B. Brandt, S. Schauermann, S. Guimond, H. Kuhlenbeck, D.E. Starr, S.K. Shaikhutdinov, J. Libuda, H.J. Freund, *Angew. Chem. Int. Ed.* 44 (2005) 7601.
- [39] A. Martínez-Arias, D. Gamarra, M. Fernández-García, X.Q. Wang, J.C. Hanson, J.A. Rodriguez, *J. Catal.* 240 (2006) 1.
- [40] M.R. Morales, B.P. Barbero, L.E. Cadús, *Appl. Catal., B* 67 (2006) 229.
- [41] N.A. Merino, B.P. Barbero, P. Grange, L.E. Cadús, *J. Catal.* 231 (2005) 232.
- [42] J.Y. Luo, M. Meng, Y.Q. Zha, L.H. Guo, *J. Phys. Chem. C* 112 (2008) 8694.
- [43] B.E. Solsona, T. Garcia, C. Jones, S.H. Taylor, A.F. Carley, G.J. Hutchings, *Appl. Catal., A* 312 (2006) 67.
- [44] G. Veser, M. Ziauddin, L.D. Schmidt, *Catal. Today* 47 (1999) 219.
- [45] M. Badlani, I.E. Wachs, *Catal. Lett.* 75 (2001) 137.
- [46] M. Skoglundh, E. Fridell, *Top. Catal.* 28 (2004) 79.
- [47] E. Finocchio, G. Busca, V. Lorenzelli, R.J. Wiley, *J. Catal.* 151 (1995) 204.
- [48] M.A. Ulla, E.A. Lombardo, *Handbook on the Physics and Chemistry of Rare Earths*, vol. 29, 2000, p. 75.